ACS OMEGA

Open Access

http://pubs.acs.org/journal/acsodf

Article

Synthesis and Characterization of Iron-Rich Glauconite Nanorods by a Facile Sonochemical Method for Instantaneous and Eco-friendly Elimination of Malachite Green Dye from Aquatic Environments

Aya Fadl Allah, Ahmed A. Abdel-Khalek, Ahmed M. El-Sherbeeny, Wail Al Zoubi,* and Mostafa R. Abukhadra*

Cite This: *ACS Omega* 2023, 8, 49347−49361

Read Online

ACCESS | Metrics & More | Article Recommendations | Supporting Information

ABSTRACT: Novel glauconite nanorods (GNRs) were synthesized by the sonication-induced chemical expansion and scrolling process of natural glauconite. The synthetic nanostructure was characterized by different analytical techniques as a superior adsorbent for the malachite green dye (MG). The synthetic GNRs were detected as porous nanorods with an average length of 150 nm to 5 μm, an average diameter of 25 to 200 nm, and a specific surface area of 123.7 m^2/g. As an adsorbent for MG, the synthetic GNRs showed superior uptake capacity up to 1265.6 mg/g at the saturation stage, which is higher than most of the recently developed highly adsorbent dyes. The adsorption behavior and mechanistic properties were depicted by using modern and traditional equilibrium modeling. The kinetic assumption of the pseudo-first-order model ($R^2 > 0.94$) and the classic isotherm of the Langmuir equilibrium model ($R^2 > 0.97$) were used to describe the adsorption reactions. The steric investigation demonstrates that each active site on the surface of GNRs can adsorb up to three MG molecules (n = 2.19−2.48) in vertical orientation involving multimolecular mechanisms. Also, the determined active site density (577.89 mg/g) demonstrates the enrichment of the surface of GNRs with numerous adsorption receptors with strong affinity for the MG dye. The energetic study, including Gaussian energy (6.27−7.97 kJ/mol) and adsorption energy (9.45−10.43 kJ/mol), revealed that GNRs had physically adsorbed the dye, which might involve electrostatic attraction, hydrogen bonding, van der Waals forces, and dipole forces. The internal energy, enthalpy, and entropy determined the exothermic and spontaneous uptake of MG.

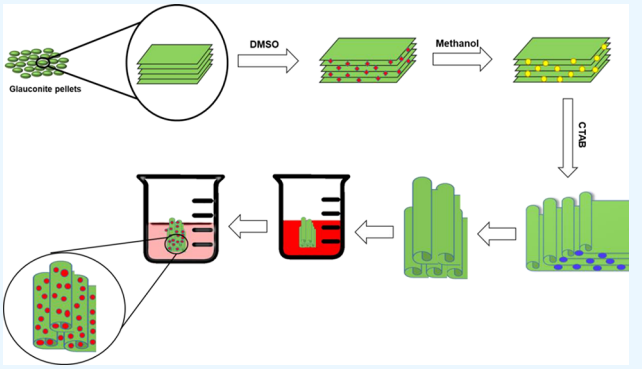

1. INTRODUCTION

In recent times, the accelerated growth of industries has resulted in significant environmental challenges, notably the issue of water pollution and its consequential impacts on both aquatic ecosystems and human health.[1,2] Various types of pollutants are discharged into the surroundings as a result of industrial operations, including dyes, pesticides, heavy metals, antibiotics, petrochemicals, and bacteria.[3,4] All of these aforementioned concerns possess substantial gravity, representing catastrophic challenges that pose a direct threat to the well-being of both human beings and all other forms of life.[5] Synthetic dyes are aromatic organic compounds that serve as crucial coloring agents for various sectors such as paper, plastic, leather, printing, and textiles.[6,7] Hence, it has been stated that an estimated quantity of over 7×10^5 tons annually of dyes manufactured is being discharged as contaminants into the natural environment and aquatic ecosystems.[8] The majority of synthetic dyes are known to possess toxicity and non-degradability, leading to a range of adverse consequences, including dermatitis, allergies, cancer, teratogenicity, skin irritation, carcinogenicity, and kidney damage.[8,9] Furthermore, the migration of dye molecules has adverse effects on the aquatic ecosystem, specifically impacting the photosynthetic activity and overall bioactivity of the species present. This pertains to the inhibitory effect of the dye surface on the penetration of sunlight into the deeper layers of water.[4,8] Malachite green (MG) is a frequently used dye, characterized as a synthetic organic molecule ($C_{23}H_{25}ClN_2$) with a green hue. However, despite the widespread use of the MG dye in several industries, including the aquaculture, food, and pharmaceutical disinfection sectors, it has been recognized as a highly hazardous compound.[4,10,11] Insufficient treatment of

Received: October 9, 2023
Revised: November 20, 2023
Accepted: November 30, 2023
Published: December 12, 2023

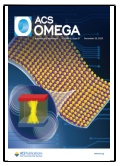

MG results in a substantial release of this molecule into the aquatic environment, leading to a decrease in the oxygen levels in the water. Moreover, the presence of MG at high concentrations poses notable health risks, including mutagenesis, pulmonary toxicity, chromosomal fractures, tumor formation, and teratogenicity.[12,13]

Consequently, a variety of investigations have been accomplished to facilitate the advancement of technology aimed at the separation of MG from water supplies. Various technologies were utilized in this study, including adsorption, ion exchange, coagulation, biological oxidation, photocatalytic oxidation, nanofiltration, flocculation, and precipitation by chemicals.[7,14] Several considerations, including simplicity, effectiveness of elimination, recycling potential, environmental significance, and maintenance prices, impose significant limitations on the prospective implementation of the aforementioned procedures in a commercial and large-scale context.[15,16] The utilization of adsorption decolorization technologies has been suggested as a viable approach due to their affordability, accessibility, safety, cost-effectiveness, and recyclability, making them suitable for large-scale applications.[17,18] Hence, a variety of efficient natural and synthetic materials have been developed with the objective of eliminating synthetic dyes from water supplies. These materials have been evaluated based on factors such as the price of production, capacity to absorb dyes, accessibility to precursors, practicality for implementation, speed of adsorption, and recyclable properties.[16,19] The utilization of effective clay-based nanostructures has proven to be an effective technique for successfully eliminating both organic and inorganic chemicals, offering the benefits of cost-effectiveness and sustainability.[3,20] Most clay minerals have flexible multilayered aluminosilicate structures with significant ion exchange capacities, considerable chemical stability, a favorable reactive surface, an excellent adsorption capacity, and thermal resistance.[21−23]

In later periods, clay-based one-dimensional nanostructures (nanotubes) have been developed as an advanced modified form of clay with unique surface area and dispersion properties.[24,25] This occurred essentially by facile sonication-prompted chemical exfoliation followed by scrolling processes, which resulted in semicrystalline particles composed of scrolled single or several clay sheets that exhibit unique surface reactivity, surface area, porous structure, and adsorption capacities.[24,26,27] However, most of the studies introduced about the exfoliation and scrolling of the clay minerals focused on both kaolinite and bentonite; no previous studies have been introduced to investigate other clay minerals, such as glauconite. Glauconite is one of the common natural clay minerals that exhibits a potassium-ferric phyllosilicate structure (K, Na) $(Fe^{3+}Fe^{2+}, Al, Mg)_2(Si,Al)_4O_{10}(OH)_2$. Structurally, glauconite is composed of mixed layers of illite/smectite intercalated units, in which the alumina dioctahedral unit is between two units of silicon tetrahedron units containing interlayer K^+ cations.[2829] Glauconite as a mineral shows significant natural reserves, low cost, metal-bearing chemical structure, attractive morphology, high surface area, promising catalytic properties, and high ion exchange capacity.[30,31] Therefore, the scrolling and exfoliation of glauconite into nanotubes will result in an innovative structure that exhibits unique physicochemical properties and adsorption capacity during the decontamination of different water pollutants.[32,33]

The introduced study involved the innovative synthesis of novel Fe-rich glauconite nanorod-like structures as superior adsorbents of malachite green dye with instantaneous removal efficiency. The evaluation of the adsorption characteristics was carried out using detailed studies, considering the main parameters and theoretical studies. The theoretical modeling involved the investigation of the classic models in addition to the advanced models to estimate the saturation adsorption capacity, active site density, number of adsorbed ions, adsorption energy, and thermodynamic functions.

2. RESULTS AND DISCUSSION

2.1. Characterization. *2.1.1. XRD Analysis.* The structural modifications as well as the dominant crystal phases were assessed based on the XRD patterns of the raw glauconite and synthetic GNRs, as well as the intermediate phases. The recognized pattern of raw glauconite significantly demonstrates the existence of glauconite as the dominant phase in addition to some impurities, which included quartz, calcite, feldspar, and hematite (Figure 1A). The identified glauconite form is

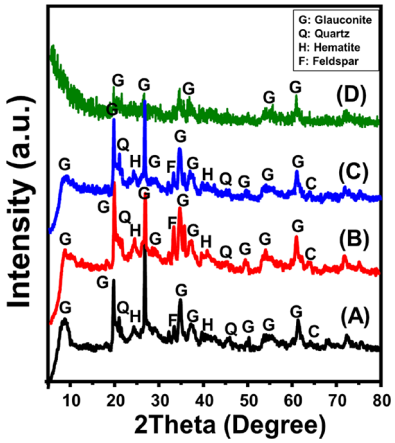

Figure 1. XRD patterns of raw glauconite (A), DMSO intercalated glauconite (B), methoxy glauconite (C), and synthetic glauconite nanorods (GNRs) (D).

represented by 1 M-glauconite poly type with a well-ordered crystalline structure of ISII ordered type and is characterized by a high K_2O content and slight swelling properties.[34] The identification of glauconite has been established by analyzing XRD peaks previously stated (8.67, 19.72, 26.7, 34.78, 37.17, and 61.31°) with basal spacing of 10.18 Å (Figure 1A).[34−36] After the modification of the glauconite with DMSO, the obtained XRD pattern demonstrates significant deviation in the essential peaks of glauconite (8.01, 19.54, 26.5, 34.5, 36.8, and 61.1°) (Figure 1B).

This validates the remarkable distortion in the structural units of glauconite after this step and the expected intercalation of the silicate layers with DMSO organic molecules. This was also signified by the detected increment in the basal spacing that expanded to 11.2 °C, demonstrating the swelling effect of the intercalated DMSO. The same observations were detected during the evaluation of the XRD pattern of methoxy glauconite (Figure 1C). The main peaks deviated to notable lower positions (7.47, 19.52, 26.5, 34.4, and 35.57°) (Figure 1C). This was also associated with a notable expansion effect on the silicate layers of glauconite, which appeared in the rise in the basal spacing to 11.81 Å. Regarding synthetic glauconite nanorods, the resulted pattern validates strong destruction of the structure units of glauconite and partial amorphization of

https://doi.org/10.1021/acsomega.3c07870
ACS Omega 2023, 8, 49347−49361

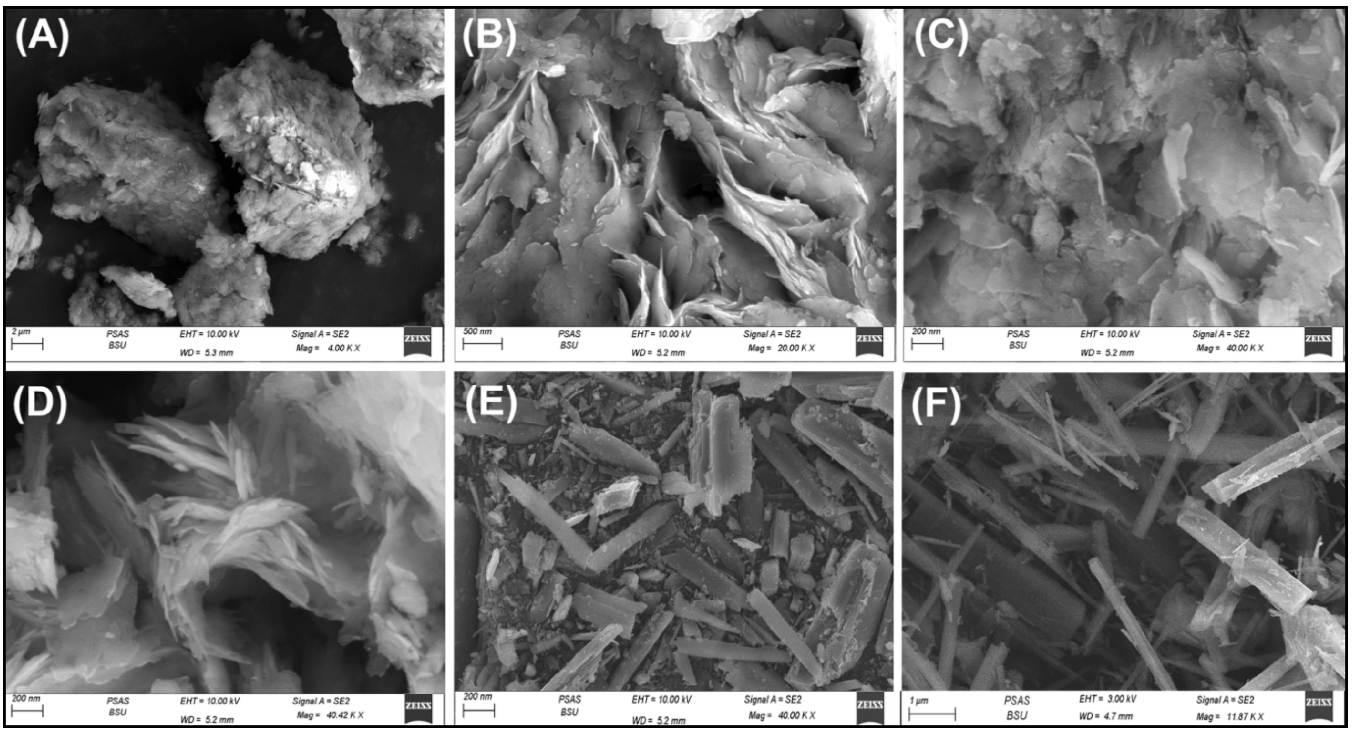

Figure 2. SEM images of raw glauconite (A), DMSO intercalated glauconite (B), methoxy glauconite (C), CTAB intercalated glauconite (D), and synthetic GNRs (E and F).

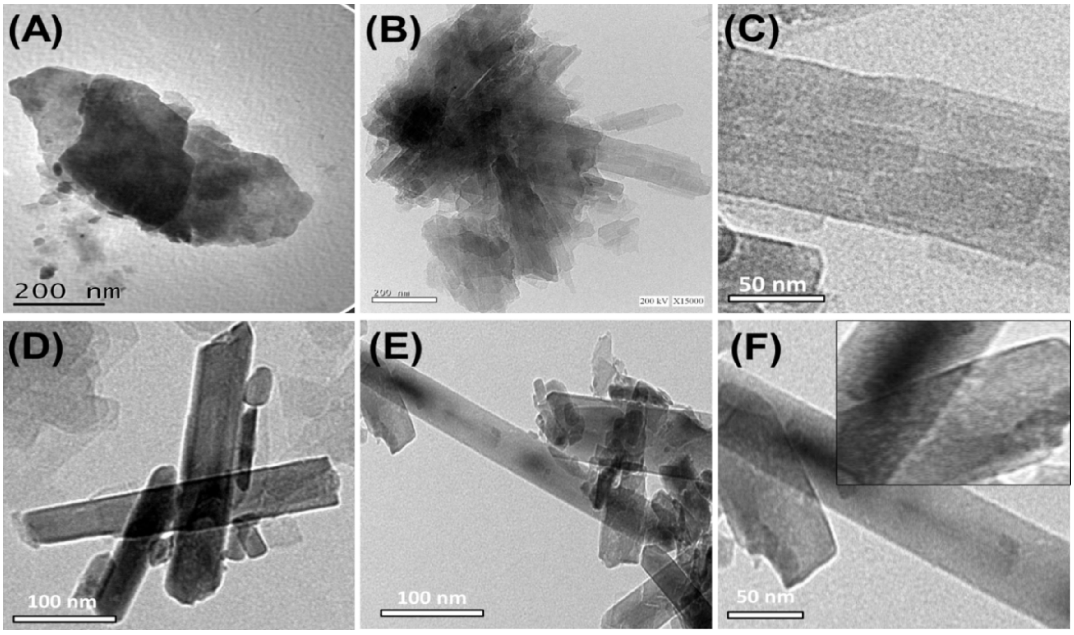

Figure 3. HRTEM images of raw glauconite (A), in-depth scrolled glauconite with lattice fingers structures (B and C), and the synthetic GNRs after extensive sonication treatment (D–F).

its structure (Figure 1D). Most of the diffraction peaks of glauconite were reduced extensively, and the main peak around 2θ of 8° completely disappeared. Additionally, this observation confirms the notable occurrence of exfoliating and separating throughout the multilayered units, leading to the development of a novel semicrystalline form.

2.1.2. SEM and HRTEM Analysis. The changes in the morphological features during the production of the glauonite nanorods were followed based on the SEM (Figure 2) as well as the HRTEM (Figure 3) images. The starting glauconite shows the common massive and agglomerated form of glauconite with the commonly detected stacky and compact layers (Figure 2A). The intercalation of the layers with DMSO molecules caused notable exfoliation of the glauconite layers, which effectively separated from each other (Figure 2B). The exfoliation steps increased significantly after the incorporation of the methanol molecules, and the glauconite samples appeared as single layers overlaid each other (Figure 2C).

https://doi.org/10.1021/acsomega.3c07870
ACS Omega 2023, 8, 49347−49361

During the initial stage of the scrolling steps and the incorporation of CTAB molecules, the separated glauconite layers exhibited slight binding and appeared in curvature form (Figure 2D). By the end of the scrolling and the modification steps in the existence of the sonication source, the sample reflects a complete change in the morphology to be in rodlike structures instead of the flaky form (Figure 2E,F). The obtained glauconite rodlike structure exhibits length within the range of 150 nm to 5 μm and diameter within the range of about 25 to 200 nm.

The recognized HRTEM images of the assessed samples confirm the detected morphological anomalies, according to the SEM images (Figure 3). The glauconite platelets appeared as massive to nearly elliptic grains without marked internal properties (Figure 3A). The intercalated CTAB molecules made the glauconite grains peel off and start to roll; they turned into a multilayered, rodlike nanostructure with clear lattice finger structures (Figure 3B,C). The extensive scrolling process, especially under the sonication effect, causes a significant condensation effect on the formed rod structure, which is in a smooth cylindrical form, suggesting separated scrolling of each layer into a single rod (Figure 3D−F). Therefore, there are no indications or observations of the previously reported lattice finger structures. However, the focus images on the surface of the finally obtained rods reflected their highly porous properties, which give the structure ribbonlike morphologies and properties, (Figure 3F). Such morphological features are associated with an increase in the surface area of the structure and its porosity, which induces its qualification to be applied as effective adsorbents for different species of dissolved water pollutants.

2.1.3. FTIR Analysis. The changes in the main chemical functionals during the synthesis steps were followed based on the observed FTIR spectra of the raw glauconite and synthetic GNRs in addition to the intermediate structures (Figure 4; Table 1). Regarding the raw glauconite, the obtained spectrum clearly displays its widely reported composition as a clay mineral with an aluminosilicate structure. These involved the identification of the corresponding bands of Si−O−Si, Fe−OH, Si−O, Si−O−Fe, Si(Al)−O-Si, and OH groups (Figure 4; Table 1). The detected hydroxyl groups around 3500 cm^{-1} were assigned to either the adsorbed water or the metal hydroxides with the glauconite structure.[37] However, the identified hydroxyl groups corresponding to the absorption band around 1600 cm^{-1} signify the interlayer free water molecules[38] (Figure 4; Table 1). Moreover, the recognized bands around 800 and 490 cm^{-1} display the enrichment of the glauconite with iron, which is in agreement with its XRF chemical analysis. Regarding the investigated spectra of both DMSO intercalated glauconite and methoxy glauconite, they show similar bands of raw glauconite with no detectable bands related to their organic structures (Figure 4; Table 1). There is only a slight fluctuation in the exact locations of the primary basic groups' matching bands, which might validate the structural effect of the intercalated organic molecules of DMSO and methanol on the structural units of glauconite (Figure 4; Table 1). Moreover, there is slight splitting for the identification band of Si(Al)−O-Si around 1000 cm^{-1}. This validates the distortion of the glauconite structural units (octahedron and tetrahedron units) as a result of the partial swelling and exfoliation of silicate layers.[39] After the formation of GNRs, the absorption bands of the main structural units of glauconite deviated at a high rate. Moreover, the splitting of the identification band of Si(Al)−O-Si around 1000 cm^{-1} increased to a considerable degree, validating an increment in distortion and exfoliation degree (Figure 4; Table 1). Moreover, new bands were detected at 1475, 2850, and 2919 cm^{-1} that strongly signify the organic structure of the CTAB molecules that were used during the exfoliation and scrolling processes (Figure 4; Table 1)

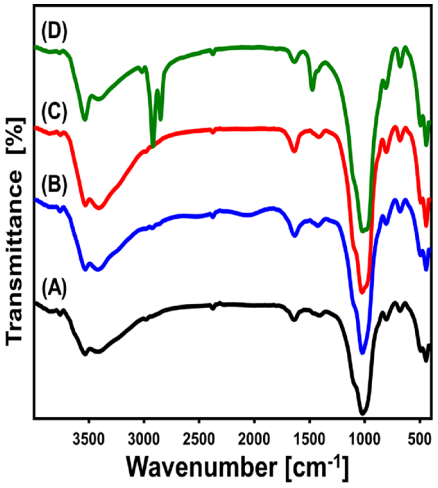

Figure 4. FTIR spectra of raw glauconite (A), DMSO intercalated glauconite (B), methoxy glauconite (C), and synthetic GNRs (D).

Table 1. FTIR Detectable Bands of Glauconite during the Various Alteration Procedures and the Corresponding Chemical Groups

absorption bands (cm^{-1})				
glauconite	DMSO/ glauconite	methoxy glauconite	GNRs	functional chemical groups
3532	3420	3530	3535	stretching and bending vibrations of −OH groups[40]
			2919	asymmetric stretching vibrations of −CH2[32]
			2850	symmetric stretching vibrations of −CH2[32]
1639	1635	1639	1638	interlayer water molecules[38]
			1475	excited methylene group[41]
1020	1022	1024	1019	Si(Al)−O−Si asymmetric stretching[3,37]
804	806	805	810	Fe_2^{3+} OH/$Fe^{2+}Fe^{3+}$OH bending[37]
681	680	681	679	bending vibration of Si−O and/or −OH[37]
493	495.6	492	495.2	Si−O−Fe^{3+}[40,42]
445.6	445.02	444	443	Si−O−Si[40,42]

2.1.4. Textural Analysis. The textural properties of the synthetic GNRs were assessed in terms of porosity and surface

The previously reported chemical findings of GNRs based on the FTIR analysis are in agreement with the recognized elemental contents determined relying upon EDX spectra (Figure 5). The essential elements of the silicate structures were detected clearly, such as O, Si, Fe, and K (Figure 5). The significant increase in the Fe content after the scrolling process of glauconite into GNRs reflected the strong diffusion of the structural ion element or iron oxide impurities during exfoliation and extensive destruction of the glauconite silicate units.

https://doi.org/10.1021/acsomega.3c07870
ACS Omega 2023, 8, 49347−49361

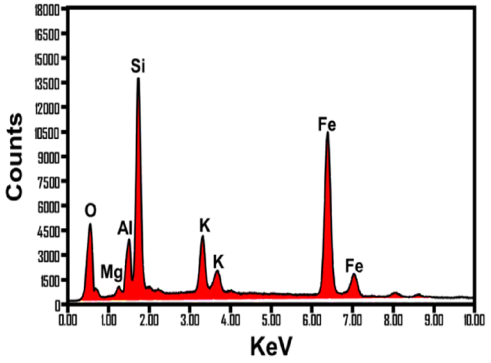

Figure 5. EDX spectrum of the synthetic GNRs and the corresponding elemental composition.

area properties based on the obtained N_2 adsorption/desorption isotherm curve (Figure 6). The observed curve

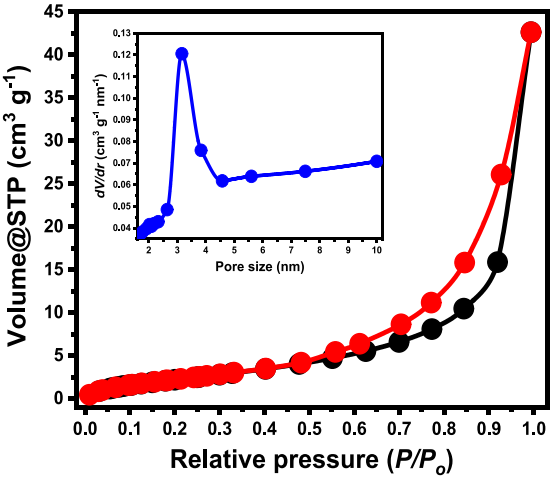

Figure 6. Plotted nitrogen adsorption/desorption isotherm curve of the synthetic GNR particles and the pore size distribution properties.

displays the IV isotherm type with a notable hysteresis loop of H3 type (Figure 6). This validates the nanoporous (mesoporous) properties of the synthetic GNRs, which are associated essentially with the evacuation and/or filling of tabular or cylindrical nanopores via capillary condensation mechanisms.[32,43] The measured surface area of GNRs is 123.7 m^2/g, which is a significantly promising value during the assessment of the product either as an ornamental or as a heterogeneous catalyst. Regarding the pore size distribution properties, the GNR particles' exhibit pore size ranges from 1.5 to 10 nm with an average pore diameter of 4.16 nm, which confirms the mesoporous structure.

2.2. Adsorption Results. *2.2.1. Influence of pH.* From pH 2 to 8, the effect of the aquatic solutions' pH on the adsorption properties of GNRs as prospective MG dye adsorbents was examined experimentally. All of these experiments were done after meticulously adjusting all of the influencing factors to set levels (MG concentration: 100 mg/L; volume: 100 mL; time: 120 min; solid dosage: 0.2 g/L; temperature: 20 °C). Based on the amounts of MG adsorbed using GNRs, there was a clear improvement when the pH of the polluted solutions tested went from 2 (20.6 mg/g) to 8 (140.8 mg/g) (Figure 7). GNRs have the ability to operate as particularly successful adsorbents throughout the real treatment efforts in line with the US EPA's

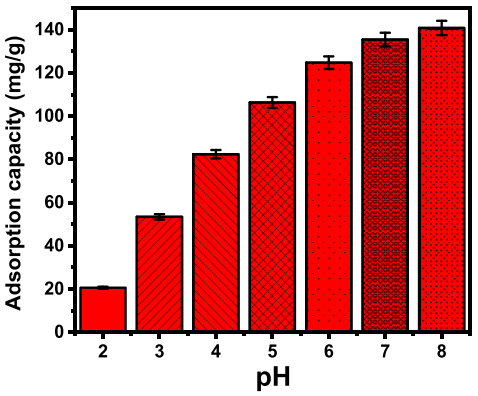

Figure 7. Influence of the solution pH on the uptake of MG dye by GNRs.

established pH limit for industrial effluents (pH 6 to 9) along with the laboratory-tested performances of GNRs at varying pH levels.[44] The investigation of the combined ionizing traits of MG dye plus the prevailing surface charges across the frameworks of GNRs may be utilized to illustrate the verified improvement in the determined adsorption behavior.

According to the pH-dependent ionization properties of MG dye, it has a pK_a value of 10.3, and it is in a stable protonated state at pH levels below this value and in a deprotonated state at pH levels above this value.[45,46] In highly acidic conditions (pH 2.0), the protonated forms (MGH^+) can be made, but in alkaline conditions, the colorless carbinol basic species can be found.[46,47] As a result, the common color of the evaluated MG dye remains stable from pH 3 toward pH 7, after which it declines dramatically with increasing solution pH upward of 11. Therefore, it is recommended to evaluate the adsorption studies in a controlled range between acidic and neutral situations.[7,45] In terms of MG ionization characteristics, its charged ions possess strong electrostatic repellence with already-existing positively energized fundamental groups of GNRs at low pH levels (acidic circumstances). The continual generation of hydroxyl anions while raising the pH of the evaluated solutions is coupled with substantial deprotonation influences on the GNRs' active groups, which are negatively charged within this pH range. As a result, the positively charged MG species are electrostatically captured in significant quantities.[43,48,49]

2.2.2. Kinetic Assessment. 2.2.2.1. Influence of Duration. The influence of the adsorbing period on the attained decolorization opportunities of MG by GNRs was investigated in a controlled investigation. The adsorption duration was varied within the range of 30−1320 min while keeping the levels of the primary influencing variables constant. These factors included the concentration of MG (100 mg/L), quantity of GNRs (0.2 g/L), volume of the solution (200 mL), temperature (20 °C), and pH (7). The decolorization properties of GNRs as potential adsorbents for MG demonstrate significant enhancements in both adsorption rates and capacities in mg/g, as well as the ability to extend the duration of the testing period in a regulated manner (Figure 8A). The effects of this enhancement may become significantly noticeable after 840 min. Subsequently, the extended period of the trials does not exhibit any significant impact on the rates of adsorption or the quantities of retained MG, indicating a state of stabilization or equilibrium conditions (Figure 8A). The particulates of GNRs in this

https://doi.org/10.1021/acsomega.3c07870
ACS Omega 2023, 8, 49347−49361

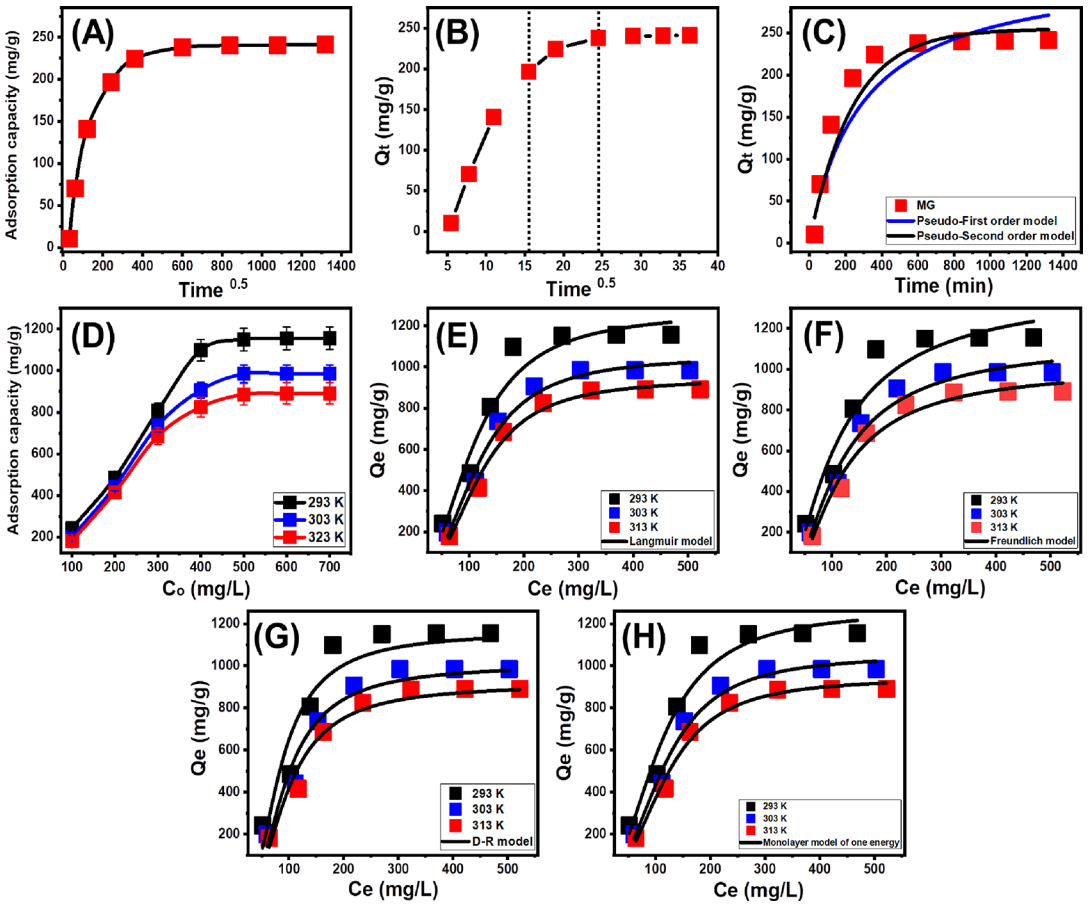

Figure 8. Influence of contact time on the uptake of MG by GNRs (A), intraparticle diffusion curve during the uptake of MG (B), fitting of the MG uptake data with the common kinetic models (C), influence of MG starting concentrations on the uptake capacities of GNRs (D), fitting of the MG uptake data with the classic Langmuir model (E), fitting of the MG uptake data with the classic Freundlich model (F), fitting of the MG uptake data with the classic D−R model (G), and fitting of the MG uptake data with the advanced monolayer equilibrium model of one site of energy (H).

specific form exhibit a certain degree of equilibrium MG dye absorption capacity at 241.3 mg/g (Figure 8A). The significant increase in the adsorption of MG and its quick rates are due to the existence of lots of unoccupied active positions on the GNR particles at the first stages of the decolorization events.[32] As the duration of testing increases, there is a progressive increase in the adsorption of MG into the unoccupied sites of GNRs. Consequently, the occupation and the increased fill of these vacant sites result in a substantial decrease in their accessibility. Therefore, there was a notable decline in the actual rates of adsorption during a certain time frame, and the GNRs demonstrated noteworthy enhancements in their adsorption properties that were overlooked. After exhaustively consuming all of the preexisting sites with the MG, researchers have successfully determined the equilibrium state of GNRs.[3]

2.2.2.2. Intraparticle Diffusion Behavior. The adsorption operations of MG utilizing GNRs exhibit an intraparticle diffusion trend demonstrating segmented characteristics consisting of three clear discrete trends that do not connect with the beginning points (Figure 8B). This finding demonstrates that the uptake of MG involves collaborative mechanisms, along with the important role that MG ion diffusion plays in the pathway of the functional sites of GNRs.[41,50] The process can involve three main mechanisms: (A) adsorption onto active sites located on the external surface, (B) diffusion within the particle, and (C) the influence of the saturation or equilibrium phase.[51] The initial phase of the experiment suggests that the external adsorption processes of MG were operational at the beginning of the testing. The efficacy of this stage is contingent upon the overall quantity of surface-active receptors (Figure 8B).[17] A subsequent phase has been discovered through the extension of time (Figure 8B), which signifies the implementation of extra mechanisms such as the influence of MG transportation operations and layered adsorption interactions.[21,51] The prevailing stage in which GNRs exist in an equilibrium state for MG adsorption has been conclusively determined. This observation provides evidence that the MG ions that were caught have entirely filled the effective receptors (Figure 8B).[16,41] The regulation of MG elimination activities during this stage is governed by a range of processes, which may involve molecular interactions and/or mechanisms such as interionic attractions.[52]

2.2.2.3. Kinetic Behaviors. The kinetic properties of the MG uptake operations by GNRs were demonstrated using the existing kinetic theories of the pseudo-first-order (P.F.) and pseudo-second-order (P.S.) models. The degree of agreement between the kinetic assumptions of the two analyzed models and our findings of MG uptake has been assessed employing standard nonlinear fitting criteria. These levels were determined based on both correlation coefficients (R^2) as well as chi-squared (χ^2) values. The results of this assessment can be found in Table 2 and are visually shown in Figure 8C.

https://doi.org/10.1021/acsomega.3c07870
ACS Omega 2023, 8, 49347−49361

Table 2. Mathematical Parameters of the Addressed Kinetic Models

kinetic models		
model	parameters	293 K
pseudo-first-order	K_1 (1/min)	0.0042
	$Qe_{(Cal)}$(mg/g)	254.8
	R^2	0.94
	X^2	3.95
pseudo-second-order	k_2(mg/g min)	1.049×10^{-5}
	$Qe_{(Cal)}$(mg/g)	330.2
	R^2	0.90
	X^2	6.23

The obtained R^2 values and χ^2 findings suggest that the characteristics and fundamental principles of the P.F. offer a more accurate representation of the MG adsorption processes by GNRs in comparison with the evaluated P.S. model. The observed agreement between the laboratory-determined capacity of GNRs at the point of equilibrium (240 mg/g) and the value predicted through theoretical approaches (254.8 mg/g) supports these findings (Table 2). The primary mechanism responsible for the sequestration of MG by GNRs, as per the principles of the P.F. model, can be attributed to physical events. These processes may involve significant contributions of van der Waals forces in addition to electrostatic attractions, as suggested by earlier investigations.[53,54] Although the equation proposed by the P.F. model for eliminating MG by GNRs is more appropriate compared with the equation offered by the P.S. theory, the uptake behaviors nevertheless exhibit substantial agreement with the kinetics of the P.S. theory. As a result, it was supposed that further frequent weakly operated chemical processes, among which are hydrogen binding, formation of complexes, and sharing of electrons, could have a secondary role or have a minimal effect on the processes.[41,53] The creation of a chemically captured MG layer was subsequently followed by the formation of a physically captured layer, employing the first chemically retained layer as the base.[55]

2.2.3. Equilibrium Investigation. 2.2.3.1. MG Concentrations. The adsorption behaviors of GNRs were investigated by varying the initial concentration of the target molecules, MG, within a range of 100 to 700 mg/L. To ensure accuracy, all relevant factors, including period (24 h), tested volume (100 mL), incorporated solid dosage (0.2 g/L), and operating temperature (293−313 K), were carefully controlled and adjusted to certain values. In the evaluation of the adsorbing aspects of GNRs, the initial concentration serves as a significant variable in elucidating equilibrium aspects and maximum capacities (Figure 8D). Upon conducting an analysis of the properties of GNRs under the influence of elevated concentrations of MG ions, a significant increase in the quantity of MG adsorption was observed (Figure 8D). The existence of increased levels of MG within certain volumes induces a significant enhancement in the migration, mobility, and driving forces of the dye ions. Consequently, this leads to increased collisions as well as chemical interactions via the binding sites located on the external surface of GNRs, thereby improving the efficiency of uptake.[41,52] The increase in the quantities of MG adsorbed in relation to the initial levels under investigation may be observed distinctly up to certain values that were evaluated (Figure 8D). Subsequently, an increase in the starting level of MG has been perceived to have a significant impact on the adsorbed quantities of MG molecules by GNRs. This effect, which has been previously overlooked, plays a crucial role in determining the equilibrium state and achieving the most favorable adsorption conditions. The equilibrium state of GNRs as adsorbents may be observed at various temperatures (293, 303, and 313 K) after being subjected to a concentration of 500 mg/L of MG. The exact performances of the GNRs for adsorbing MG are measured to be 1156, 985.1, and 890.2 mg/g at the respective temperatures (Figure 8D). The diminution in the adsorption of MG via

Table 3. Statistical Parameters of the Conventional and Modern Isotherm Models

conventional isotherm				
		293 K	303 K	313 K
Langmuir model	Q_{max}(mg/g)	1266.8	1052.42	942.63
	b (L/mg)	3.35×10^{-5}	1.03×10^{-5}	7.09×10^{-6}
	R^2	0.976	0.988	0.991
	X^2	3.29	1.66	1.02
Freundlich model	$1/n$	0.709	0.623	0.598
	k_F(mg/g)	125.09	320.9	447.6
	R^2	0.932	0.970	0.976
	X^2	5.39	2.22	2.34
D−R model	β (mol^2/kJ^2)	0.00787	0.00866	0.0127
	Q_m(mg/g)	1162.3	1006.8	912.8
	R^2	0.912	0.96	0.971
	X^2	7.31	3.64	3.02
	E (kJ/mol)	7.97	7.59	6.27
Advanced isotherm				
monolayer model of one energy	R^2	0.982	0.988	0.992
	X^2	1.74	1.089	0.428
	n	2.19	2.41	2.48
	Nm (mg/g)	577.89	435.38	379.39
	Q_{Sat} (mg/g)	1265.6	1049.2	940.8
	ΔE (kJ/mol)	−9.45	−9.97	−10.43

https://doi.org/10.1021/acsomega.3c07870
ACS Omega 2023, 8, 49347−49361

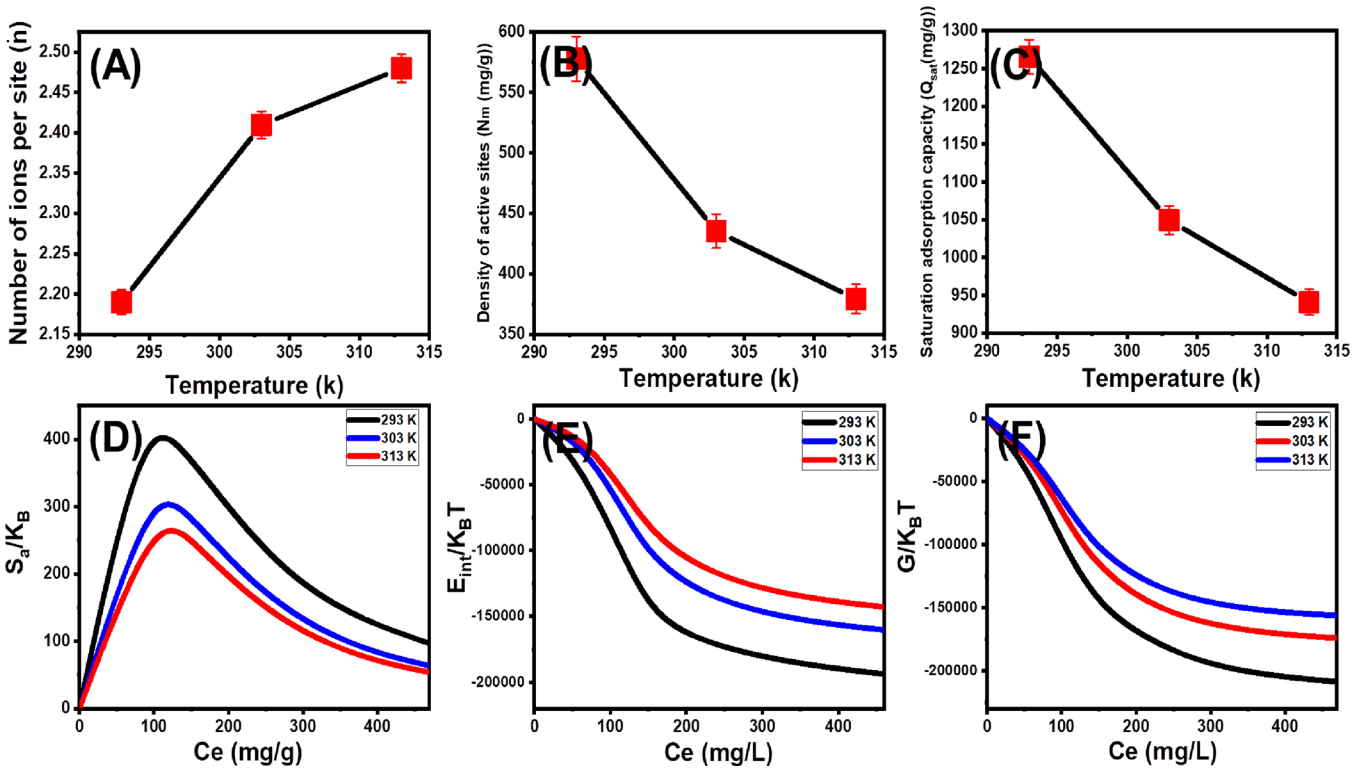

Figure 9. Variations in the quantity of MG molecules retained per site over the surface of GNRs (A), variations in the density of active sites with regard to temperature (B), fluctuations in the predicted uptake capacity of MG during the point of saturation of GNRs (C), shifts in entropy values in relation to MG concentration as well as temperature (D), variations in internal energy values with respect to MG concentration alongside temperature (E), and variations in enthalpy values as a function of MG concentration alongside temperature (F).

GNRs that can be observed in the context of the experiment's temperature suggests that the processes were exothermic.

2.2.3.2. Giles's Classification. The MG equilibrium graphs were categorized using GNRs according to the criteria established by Giles's classification. The analysis showed that these curves exhibited an L-type equilibrium behavior, as depicted in Figure 8D.[56] The equilibrium aspects of the L-type play a crucial role in the profound effects resulting from intermolecular attraction forces during the adsorption stages of MG via GNR particulates. These effects are further amplified by the intense interactions between MG molecules and the framework of GNR particulates that is highly reactive.[57] Based on the properties of the L-type isotherm, it was possible that a complete formation of an adsorbed MG monolayer would occur on the exterior interfaces of GNR particles.[58] Moreover, the observed isothermal activity implies that the GNR nanostructures have been improved by the incorporation of a variety of activated and empty uptake sites. These receptors demonstrate significant selectivity toward the target molecules, specifically the MG compounds, during the adsorption process, especially when the initial levels are low.

2.2.3.3. Conventional Isotherms. The equilibrium assessments of the MG elimination pathways by GNRs nanoparticles were investigated by using the key principles of the traditional Langmuir, Freundlich, and Dubinin–Radushkevich (D–R) hypotheses. Nonlinear regression modeling was used to evaluate the congruence that exists between the isotherm assumptions of various models and measured findings, employing illustrative mathematical equations. The assessment relied on the determination coefficient (R^2) alongside the chi-squared (χ^2) statistic. The assessment is displayed in Table 3 and depicted in Figures 8E–G. The results obtained from the analysis of R^2 and χ^2 that indicate that the MG retained actions via the GNR nanostructures align more closely with the basic concepts of the Langmuir isotherm (Figure 8E; Table 3) instead of the fundamental properties of the Freundlich isotherms (Figure 8F; Table 3). The Langmuir equation depicts the uniform distribution of MG adsorption onto GNR nanoparticles, specifically targeting the empty and active sites and forming a monolayer arrangement.[53,54] Further, it has been observed that the calculated RL value of the MG adsorption actions facilitated by the GNR nanostructures is below 1. This suggests that the reactions exhibit desirable characteristics, as indicated by previous studies.[16,17] The anticipated maximum absorption capacities (Qe_{max}) of GNRs at different temperatures are as follows: 1266.8 mg/g at 293 K, 1052.42 mg/g at 303 K, and 942.63 mg/g at 313 K, as indicated in Table 3.

The fundamental concepts of the D–R model's isotherm, as depicted in Figure 8G, elucidate the energy variations of GNRs nanomaterials while they undergo the process of capturing the MG dye. These energy variations remain unaffected by the surface features of the particles, which can either be heterogeneous or homogeneous.[59] The theoretically defined parameter known as Gaussian energy (E), determined from the D–R assessment approach, plays a crucial role in determining the sort of MG uptake mechanisms that are affecting it, i.e., whether they are chemical pathways or physical behaviors. Processes characterized by energies (E's) of below 8 kJ/mol, spanning from 8 to 16 kJ/mol, and over 16 kJ/mol are suggestive of distinguishable physical, poor chemical to complex (physical and weak chemical), and forceful chemical specifications, respectively.[16,59] The obtained E values using

https://doi.org/10.1021/acsomega.3c07870
ACS Omega 2023, 8, 49347–49361

GNRs were verified to fall inside the allowed energy limits of physical activities (<8 kJ/mol) (Table 3).

2.2.3.4. Advanced Isotherm Modeling. The investigation of advanced equilibrium models that are in accordance with the principles of statistical physics concepts can yield valuable insights into specific features of adsorption operations, particularly in terms of the interfaces between the adsorbent and adsorbate as well as the exterior properties of the solid particles involved. The numerical parameters obtained from these models, including the energetic and steric elements, have the opportunity to be used to highlight the mechanistic processes. The steric components included three key parameters: the quantity of functionally active sites on GNRs filled with the target molecule of MG ($Nm_{(MG)}$), the total amount of MG molecules captured by every site ($n_{(MG)}$), and the maximum absorption capacity of GNRs under a saturated state (Q_{sat}). The energetic parameters considered in this study were the energy required for MG elimination (ΔE), the internal energy (E_{int}), the free enthalpy (ΔG), and the entropy (Sa). A computational model of MG uptake processes has been conducted using nonlinear fits and the illustrated equations corresponding to these models. The achievement of this task was facilitated by the use of multivariable nonlinear regression simulations in conjunction with the Levenberg−Marquardt iterating approach. The MG adsorption procedures by GNRs were shown using a monolayer model that had a single energy site (Table 3; Figure 8H).

Steric Parameters

Number of Retained MG (n) at a Single Site

The numerical results of the $n_{(MG)}$ factor strongly indicate the manner in which the MG ions have been adsorbed on the outermost layers of the GNRs, either vertically or horizontally. Additionally, these values provide insights into the mechanistic pathways involved, namely, if there are multidocking processes or multi-interaction mechanisms occurring. The procedures most affected by multidocking pathways involve the acquisition of many MG molecules through the binding of several uptake receptors in horizontal arrangements. The retention mechanisms of the ions with a value of less than 1 are linked to the horizontal configuration of the ions that are bonded. On the other hand, systems exhibiting values greater than 1 exhibit both nonparallel and vertical alignment for the retained MG. The observed uptake operations in these systems are predominantly regulated by multi-ionic pathways that entail the binding of numerous dyes into a single site.[16,60] The observed levels of $n_{(MG)}$ all over the process of MG capture by GNRs (with a range of n values between 2.19 and 2.48) exhibit values that surpass 1, as depicted in Figure 9A and Table 3. Consequently, the MG molecules were adsorbed through multi-ionic mechanistic steps, wherein each adsorption site of the GNRs had the capacity to accommodate up to three ions and exhibited a vertical orientation with nonparallel characteristics. In the context of temperature implications, the calculated values of $n_{(MG)}$ for GNRs provide confirmation that they are pertaining to the temperature rise from 293 to 313 K (Figure 9A). The observed phenomenon of increased aggregation aspects of the MG immediately following its adsorption onto GNRs at higher temperatures has frequently been ascribed to this factor.[61] Furthermore, the aforementioned observation serves as evidence for the existence of thermal activation actions that occur prior to the capture of MG by GNRs.[2,62,63]

Occupied Receptor Density (Nm)

The density of MG-filled receptors (Nm) on GNRs is a significant indicator of the overall number of available and effective retention sites on the surfaces of the nanoparticles involved in the chemical reaction (Figure 9B and Table 3). The predicted $Nm_{(MG)}$ values of GNRs at different temperatures, specifically 577.89 mg/g (293 K), 435.4 mg/g (303 K), and 379.4 mg/g (313 K), exhibit considerable promise when compared to previous research on clay minerals in general and their transformed frameworks. The $Nm_{(MG)}$ values of GNRs exhibit temperature-dependent irreversible relationships (Figure 9B; Table 3). The measured values of $n_{(MG)}$ align with this finding, as an increase in aggregation affinities leads to a decrease in the total number of filled sites. Additionally, the temperature has an impact on the dominant condition of the sites that are filled.[2,64] The application of high-temperature conditions has been found to have a positive impact on the activation of uptake sites for GNRs. This effect can be attributed to the exposure of further active sites as well as the presence of new energetic site groups.[64,65] There is a direct relationship between the increase in adsorption temperature and the decrease in the viscosity level of the MG solutions.[66] Consequently, the mobility and diffusion activity of water-soluble MG molecules exhibit a significant increase upon interaction with additional reactive sites.

Saturation Adsorption Properties (Q_{sat})

The saturation level of the MG sequestered effectiveness of GNRs, denoted as Q_{sat}, represents the most reliable estimate for the maximum quantity of MG that can be adsorbed. The amounts of Q_{sat} are impacted by two main factors, which are the total quantity of retained MG molecules per site ($n_{(MG)}$) along with the formerly calculated densities of the filled sites ($Nm_{(MG)}$). GNRs exhibit significant potential as a highly effective adsorbent for the adsorption of MG. The Q_{sat} (saturated adsorption capacities) values of GNRs at various temperatures have been calculated to be 1265.6 mg/g at 293 K, 1049.2 mg/g at 303 K, and 940.8 mg/g at 313 K. The exothermic characteristics of the MG-capturing activities by GNRs are affected by the adverse impact of temperature (Figure 9C; Table 3). Additionally, this finding suggests that the impact of the temperature at which the adsorption process occurs on thermal collisions is increasing, resulting in a decline in the effectiveness of MG sequestration.[60] Furthermore, the observed characteristics of Q_{sat}, which are driven by temperature adsorption, are consistent with the previously established patterns of $Nm_{(MG)}$ instead of $n_{(MG)}$. This suggests that the effectiveness of adsorption is impacted by the abundance of vacant sites in contrast to every active site's distinctive capacity.

Energetic Assessment

Uptake Energy

The energy changes (ΔE's) associated with the uptake processes of MG exhibit regular patterns that may be attributed to either chemical or physical triggers. The physical processes that exert influence exhibit energy levels below 40 kJ/mol, but the chemical pathways possess levels of energy over 80 kJ/mol. The categorization of physically occurring mechanistic activities is dependent on adsorption energy levels. The aforementioned interactions encompass coordination exchanges (40 kJ/mol), forces of dipole bonding (2−29 kJ/mol), hydrogen bonds (<30 kJ/mol), van der Waals forces (4−10 kJ/mol), and hydrophobic bonds (5 kJ/mol).[61,64] The computational estimation of the uptake energy by MG (ΔE) was performed using eq 1, which incorporates the solubility factors of MG in water (S), the gas constant (R = 0.008314 kJ/

https://doi.org/10.1021/acsomega.3c07870
ACS Omega 2023, 8, 49347−49361

mol·K), the MG level during the half-saturating state of GNRs, and the absolute temperature (T).[65]

$$\Delta E = RT\ln\left(\frac{S}{C}\right) \quad (1)$$

The energy estimations for MG capture by GNRs fall inside the range of −9.45 to −10.43 kJ/mol, as seen in Table 3. Hence, the primary mechanisms behind the absorption of MG by GNRs may be attributed to physical phenomena, particularly van der Waals forces (ranging from 4 to 10 kJ/mol), dipole bonding forces (ranging from 2 to 29 kJ/mol), and hydrogen binding forces (below 30 kJ/mol). Moreover, the observed negative signs of ΔE throughout the sequestration of MG by GNRs are consistent with formerly described experimental findings, indicating that the underlying mechanisms are exothermic.

Thermodynamic Investigations

Entropy (S_a)

The S_a properties of the MG sequestration operations by GNRs effectively demonstrate the characteristics of order and disorder on the exterior surfaces of these particles when exposed to different levels of dye ions as well as the specified reaction temperature. The properties of S_a have been examined based on the results obtained from eq 2, employing the aforementioned documented values for $Nm_{(MG)}$ and $n_{(MG)}$, together with the expected level of MG after the half-saturation phase of GNRs (C1/2).

$$\frac{S_a}{K_B} = \mathrm{Nm}\left\{\ln\left(1+\left(\frac{C}{C_{\frac{1}{2}}}\right)^n\right) - n\left(\frac{C}{C_{\frac{1}{2}}}\right)^n \frac{\ln\left(\frac{C}{C_{\frac{1}{2}}}\right)}{1+\left(\frac{C}{C_{\frac{1}{2}}}\right)^n}\right\} \quad (2)$$

Based on the obtained data, it can be noted that the entropy levels (S_a's) exhibit a notable decrease throughout the process of MG adsorption by GNRs, particularly in the experiments conducted with very high concentrations of MG (Figure 9D). The observed trend demonstrates a significant reduction in the disorder features of the interfaces of GNR particulates as the levels of MG rise. Furthermore, the entropy functions further support the effective docking of the MG inside the existing inactive and unbound interaction receptors of the GNRs in the context of slightly lower concentrations of the dye molecules.[61,65] The experimental results shown in Figure 9D indicate that the maximum entropy values were seen when MG was captured by GNRs at equilibrium concentrations of 116.9 (at a temperature of 293 K), 111.5 (at a temperature of 303 K), and 102.8 mg/L (at a temperature of 313 K). The equilibrium levels of MG observed in this study exhibit a notable resemblance to the expected values for GNRs during their half-saturation phases. Consequently, the surplus of MG ions is unable to bind to the unoccupied locations of GNRs. Furthermore, the conspicuous reductions in the reported entropy suggest a noteworthy decrease in the quantity of accessible sites accompanied by a major loss in the degrees of freedom and diffusion characteristics of the MG ions.[66,67]

Internal Energy and Free Enthalpy Characteristics

The present study assessed the internal energy (E_{int}) associated with the sequestration of MG via GNRs as well as the changes in free enthalpy (G) resulting from variances in dye concentration as well as operational temperature. These evaluations were conducted using values obtained from eqs 3 and 4, which were computed using previously established parameters including $Nm_{(MG)}$, $n_{(MG)}$, $C_{1/2}$, and the translation partition (Z_v).[65]

$$\frac{E_{int}}{K_B T} = nN_m\left[\left(\frac{\left(\frac{C}{C_{1/2}}\right)^n \ln\left(\frac{C}{Z_v}\right)}{1+\left(\frac{C}{C_{1/2}}\right)^n}\right) - \left(\frac{n\ln\left(\frac{C}{C_{1/2}}\right)\left(\frac{C}{C_{1/2}}\right)^n}{1+\left(\frac{C}{C_{1/2}}\right)^n}\right)\right] \quad (3)$$

$$\frac{G}{K_B T} = nN_m \frac{\ln\left(\frac{C}{Z_v}\right)}{1+\left(\frac{C_{1/2}}{C}\right)^n} \quad (4)$$

The calculated internal energy (E_{int}) values for the MG sequestration activities by GNRs possess negative signals. Notably, these findings demonstrate a significant decrease as long as the temperature increases from 293 to 303 K (Figure 9E). This finding adds further evidence to the exothermic along with intrinsically spontaneous character of the MG removal mechanisms by GNRs. Consistent patterns of reactions and characteristics have been noticed in connection with the predetermined levels of S_a. The G values are characterized by negative signals and demonstrate a reversible dependence on the sequestration temperature under the test. This supports the spontaneity and exothermic character of the MG retention by GNRs and points to a decline in the feasibility characteristics (Figure 9F).

2.2.4. Recyclability. The investigation of the possibility of GNRs as a reusable adsorbent for the efficient elimination of MG dye has been conducted considering its significance in the assessment of the product for commercial and practical uses. The GNR nanoparticles utilized in the study underwent an intensive rinsing procedure using distilled water for a duration of 10 min, which was repeated five times. The purified GNRs were afterward subjected to a drying process at a temperature of 60 °C for a duration of 8 h. This was done to prepare them for further use in additional cycles of MG adsorption. The conducted recyclability studies were performed while considering the variables of adsorption under a pH of 8, a dose of 0.20 g/L for GNRs, a concentration of 100 mg/L for MG, an interval of 24 h, an overall volume of 100 mL, and a temperature of 293 K. Based on the six cycles conducted to assess the recycling potential, the use of GNRs as the adsorbent demonstrates significant stability and exceptional qualities for recyclability, as shown by the achieved efficacy of MG adsorption (Figure 10). The recyclable properties of GNRs resulted in varying levels of adsorption performance throughout the six rounds. The adsorption performance values were 241.3 mg/g (cycle 1), 238.7 mg/g (cycle 2), 230.2 mg/g (cycle 3), 218.4 mg/g (cycle 4), 200.7 mg/g (cycle 5), and 178.5 mg/g (cycle 6) (Figure 10). The repeated recycling of GNRs leads to slight decreases in the observed adsorption capabilities of MG. The observed behavior could possibly be attributed to the anticipated reduction in the quantity of GNR nanoparticles throughout the washing steps or the ongoing formation of complexes between the chemical structure of the MG molecule and the structural framework of the GNRs.

2.2.5. Comparison Study. The calculated capacity of the GNR adsorbent has been compared to other explored adsorbents in the literature (Table S3). The results reveal that GNRs have a higher capacity than the other materials, which include clay-based adsorbents, graphene oxide/Fe_3O_4

https://doi.org/10.1021/acsomega.3c07870
ACS Omega 2023, 8, 49347−49361

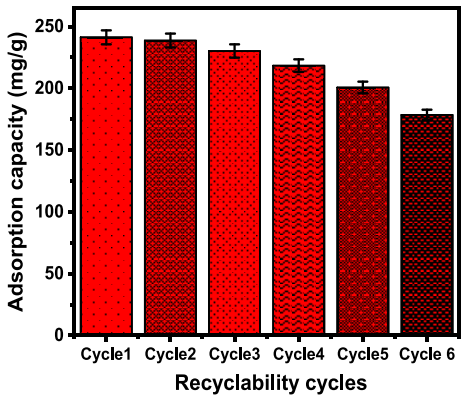

Figure 10. Recyclability properties of the synthetic GNRs during the uptake of MG dye.

composites, nZVI/BC composite, $Sr_5xBa_3x(PO_4)_3(OH)/Fe_3O_4$, mesoporous carbon, sulfonated coal, magnesium hydroxyapatite, activated carbon, activated carbon, hydroxyl functionalized coal, chitosan/poly(acrylic acid)/bentonite, and halloysite nanotubes (Table 4). This supports the significance of the produced structure as an improved adsorbent with high adsorption performance, simple synthesis approaches, excellent recyclability, cheap cost, and readily available precursors.

Table 4. Comparison between the MG Uptake Capacity of GNRs and Other Studied Adsorbents in the Literature

adsorbents	Q_{max} (mg/g)	references
activated carbon	395	68
chitosan/poly(acrylic acid)/bentonite	454.5	69
nZVI/BC composite	515.77	11
MAL	456.62	70
rGO	476.2	71
SS.C (Q_{max})	454.34	4
FHAP-SH	625	72
Artocarpus odoratissimus leaves	422	73
$Sr_5xBa_3x(PO_4)_3(OH)/Fe_3O_4$	526	47
Fe_3O_4/PT/GO	560.5	74
$Mg.HPA_{NFs}$ (Q_{max})	710.93	7
hydroxyl functionalized coal	763	19
mesoporous carbon	476.1	75
GNRs	1265.6	this study

3. CONCLUSIONS

A novel nanostructure of glauconite nanorods (GNRs) was synthesized effectively with an average diameter of 25−200 nm, an average length of 150 nm−5 μm, a BET surface area of 123.7 m^2/g, and an average pore diameter of 4.16 nm. The formation of GNRs as mesoporous nanostructures was confirmed by different analytic techniques, including XRD, SEM, HRTEM, and BET. As an adsorbent of MG dye, it displays a strong adsorption capacity (1265.6 mg/g) compared to numerous studied adsorbents. This was assigned to its high surface area, high surface reactivity, and significant existence of numerous active sites (active site density = 577.89 mg/g). Monolayer and homogeneous uptake of MG on the surface of GNRs was concluded depending on the adsorption's strong match with the Langmuir theory. Moreover, the number of adsorbed MG ions per site ($n > 1$) depicts how the adsorbed ions are oriented vertically by multimolecular mechanistic pathway. According to the energetic study (Gaussian energy (6.27−7.97 kJ/mol) alongside uptake energy (9.45−10.43 kJ/mol) together with the thermodynamic characteristics, MG sequestration by GNRs has taken place spontaneously via exothermic and physical processes.

4. EXPERIMENTAL WORK

4.1. Materials. The natural glauconite mineral was obtained from the El-Gedida area, El-Bahariya Oasis, Western Desert, Egypt. The studied sample displayed a chemical composition that consisted of SiO_2 (52.2%), Fe_2O_3 (23.14%), K_2O (6.48%), Al_2O_3 (6.12%), MgO (3.53%), CaO (0.27%), SO_3 (0.17%), P_2O_5 (0.10%), Na_2O (0.08%), TiO_2 (0.11%), MnO (0.01%), and 7.8% L.O.I. Cetyltrimethylammonium bromide (CTAB) (>98%), dimethyl sulfoxide (DMSO) (>99.5%), NaOH (97%), and methanol (>99.9%) were acquired from Sigma-Aldrich, Egypt, and were used in the glauconite transformation process.

4.2. Synthesis of Glauconite Nanorods (GNRs). The synthesis of the glauconite nanorods was produced according to the reported scrolling procedures by Abukhadra et al.[32] About 40 g of the starting glauconite mineral, after extensive grounding, was dispersed in 200 mL of diluted DMSO solution (80% DMSO/10% water) under vigorous stirring for 72 h. This particular procedure is of the greatest significance in the process of breaking the intermolecular bonds present within the layers of clay, especially the illite units of the glauconite structure. After that, the formed product was washed by methanol for five runs, and each washing run continued for about 20 min, forming methoxy glauconite (MX/G) with organophilic properties. The obtained MX/G fractions were immersed in aqueous solutions of CTAB as an expansion reagent (60 g in 200 mL) at room temperature under continuous stirring for 48 h at 1000 rpm to achieve successful exfoliation of the glauconite sheets. After that, the system was treated by sonication waves for 96 h in the presence of a sonication source of 240 W power supply to guarantee the rolling of the exfoliating layers into glauconite rods. The product after that was extracted by filtration using Whitman filter paper, washed several times with distilled water, and finally dried at 60 °C to be applied in further characterization steps.

4.3. Characterization Instruments. The crystal forms and crystallization properties were assessed and analyzed based on the X-ray diffraction (XRD) patterns of the prepared materials using a PANalytical-Empyrean X-ray diffractometer with a detection range spanning from 0 to 70°. The change in the structural chemical groups during the production steps was estimated using a Shimadzu FTIR-8400S spectrometer covering the detection range of 400 until 4000 cm^{-1}. The surficial characteristics of the resulting structures, together with the initial glauconite, were analyzed using a Gemini Zeiss Ultra 55 scanning electron microscopy. The materials being studied were made ready by spraying their surfaces with gold films immediately before imaging. Moreover, their internal structures and scrolling features were subsequently observed using HRTEM photos, which were gathered employing a transmission electron microscope (JEOL-JEM2100) with an accelerating voltage of 200 kV. The degrees of porosity along with specific surface area were determined by employing a surface area analyzer (Beckman Coulter SA3100) immediately following the degassing of the specimens. The assessment has

https://doi.org/10.1021/acsomega.3c07870
ACS Omega 2023, 8, 49347−49361

been accomplished based on the well-established N_2 adsorption and desorption isotherms.

4.4. Batch MG Adsorption Experiments. The adsorption tests of MG dye by the synthetic GNRs were studied in batch form considering the impact of pH (2−9), dye concentration (100−1000 mg/L), and adsorption duration (30−900 min). These tests were performed in triplicate considering the fixed volume of the treated dye solutions (100 mL) and certain GNR dosages (0.2 g/L). The adsorption equilibrium tests were assessed at different temperature conditions (308, 318, and 323 K). By completing the equilibration interval of each test, the water samples after the tests were filtrated by Whitman filter paper (40 μm) to remove the incorporated GNR fractions and to test the remaining concentration of the dye in the solutions. The remaining MG concentrations after the treatment steps were determined using a UV−vis spectrophotometer, and the values were applied in the calculation of the MG adsorption capacity of GNRs according to eq 5. The Q_e, C_o, C_e, V, and m symbols in the equation identify the GNR adsorption capacity (mg/g), starting MG concentration (mg/L), rest MG concentration (mg/L), tested volume of MG aqueous solution (mL), and GNR dosage (mg).

$$Q_{e(mg/g)} = \frac{(C_o - C_e)V}{m} \quad (5)$$

4.5. Conventional and Modern Equilibrium Investigations. The adsorption of MG via GNRs were illustrated according to the commonly applied classic kinetics, classic isotherm, and advanced isotherm studies based on the theoretical statistical physics theory (Table S1). The studied kinetic and traditional isotherm models were evaluated based on the recognized nonlinear fitting degrees of the performed MG adsorption results, considering the values of both the determined coefficient (R^2) (eq 6) and chi-square (χ^2) (eq 7). About the nonlinear fit levels involving the simulated isotherm models' explanatory formulas and the MG decontamination findings, they were assessed on the basis of both the determination coefficient (R^2) and root-mean-square error (RMSE) (eq 8). The incorporated m', p, Qi_{cal}, and Qi_{exp} in the equation refer to the MG uptake results, uptake parameters, calculated MG uptake capacity, and measured MG uptake capacity, respectively.

$$R^2 = 1 - \frac{\sum (Q_{e,exp} - Q_{e,cal})^2}{\sum (Q_{e,exp} - Q_{e,mean})^2} \quad (6)$$

$$\chi^2 = \sum \frac{(Q_{e,exp} - Q_{e,cal})^2}{Q_{e,cal}} \quad (7)$$

$$RMSE = \sqrt{\frac{\sum_{i=1}^{m} (Qi_{cal} - Qi_{exp})^2}{m' - p}} \quad (8)$$

■ ASSOCIATED CONTENT

Supporting Information

The Supporting Information is available free of charge at https://pubs.acs.org/doi/10.1021/acsomega.3c07870.

Representative equations of the kinetic and isotherm models (Table S1) (PDF)

■ AUTHOR INFORMATION

Corresponding Authors

Wail Al Zoubi − *Materials Electrochemistry Laboratory, School of Materials Science and Engineering, Yeungnam University, Gyeongsan 38541, Republic of Korea;* orcid.org/0000-0003-4213-8481; Email: wailalzoubi@ynu.ac.kr

Mostafa R. Abukhadra − *Materials Technologies and their Applications Lab, Geology Department, Faculty of Science, Beni-Suef University, Beni-Suef City 62511, Egypt; Geology Department, Faculty of Science, Beni-Suef University, Beni-Suef City 62511, Egypt;* orcid.org/0000-0001-5404-7996; Email: Abukhadra89@Scinec.bsu.edu.eg

Authors

Aya Fadl Allah − *Materials Technologies and their Applications Lab, Geology Department, Faculty of Science, Beni-Suef University, Beni-Suef City 62511, Egypt; Department of Chemistry, Faculty of Science, Beni-Suef University, Beni-Suef City 62514, Egypt*

Ahmed A. Abdel-Khalek − *Department of Chemistry, Faculty of Science, Beni-Suef University, Beni-Suef City 62514, Egypt*

Ahmed M. El-Sherbeeny − *Industrial Engineering Department, College of Engineering, King Saud University, Riyadh 11421, Saudi Arabia;* orcid.org/0000-0003-3559-6249

Complete contact information is available at: https://pubs.acs.org/10.1021/acsomega.3c07870

Author Contributions

This article was written through the contributions of all authors. All authors have given approval to the final version of the manuscript.

Notes

The authors declare no competing financial interest.

■ ACKNOWLEDGMENTS

This publication is funded through the United States Agency for International Development (USAID). The contents are the responsibility of the authors and do not necessarily reflect the views of USAID or the United States Government. Also, the authors extend their appreciation to King Saud University for funding this work through Researchers Supporting Project number (RSP2023R133), King Saud University, Riyadh, Saudi Arabia.

■ REFERENCES

(1) Sajid, M.; Sajid Jillani, S. M.; Baig, N.; Alhooshani, K. Layered Double Hydroxide-Modified Membranes for Water Treatment: Recent Advances and Prospects. *Chemosphere* **2022**, *287*, No. 132140.

(2) Yang, X.; Wang, J.; El-Sherbeeny, A. M.; AlHammadi, A. A.; Park, W.-H.; Abukhadra, M. R. Insight into the Adsorption and Oxidation Activity of a ZnO/Piezoelectric Quartz Core-Shell for Enhanced Decontamination of Ibuprofen: Steric, Energetic, and Oxidation Studies. *Chemical Engineering Journal* **2022**, *431*, No. 134312.

(3) Abdel Salam, M.; Mokhtar, M.; Albukhari, S. M.; Baamer, D. F.; Palmisano, L.; Jaremko, M.; Abukhadra, M. R. Synthesis and Characterization of Green ZnO@polynaniline/Bentonite Tripartite Structure (G.Zn@PN/BE) as Adsorbent for As (V) Ions: Integration, Steric, and Energetic Properties. *Polymers* **2022**, *14* (12), 2329.

(4) AlHammadi, A. A.; Nasser, R.; Shaban, M. S.; Othman, S. I.; Khim, J. S.; Ajarem, J. S.; Allam, A. A.; Abukhadra, M. R. Insight into the Effect of Sulfonation Techniques on the Adsorption Properties of

https://doi.org/10.1021/acsomega.3c07870
ACS Omega 2023, 8, 49347−49361

– SO3H Surface-Functionalized Coal as Adsorbent for Malachite Green Dye: Steric and Energetic Investigation. *ACS Omega* **2022**, *7* (41), 36697−36711.
(5) Benisha, R.; Amalanathan, M.; Aravind, M.; Mary, M. S. M.; Ahmad, A.; Tabassum, S.; Al-Qahtani, W. H.; Ahmad, I. Catharanthus Roseus Leaf Extract Mediated Ag-MgO Nanocatalyst for Photocatalytic Degradation of Congo Red Dye and Their Antibacterial Activity. *J. Mol. Struct.* **2022**, *1262*, No. 133005.
(6) Taher, T.; Putra, R.; Rahayu Palapa, N.; Lesbani, A. Preparation of Magnetite-Nanoparticle-Decorated NiFe Layered Double Hydroxide and Its Adsorption Performance for Congo Red Dye Removal. *Chem. Phys. Lett.* **2021**, *777*, No. 138712.
(7) Okasha, A. T.; Abdel-Khalek, A. A.; El-Sherbeeny, A. M.; Zoubi, W. A.; Abukhadra, M. R. Advanced Equilibrium Study on the Synthesis and Characterization of Mg-Doped Hydroxyapatite Nano-Fibers as a Potential Enhanced Adsorbent of Zn (II) and Malachite Green Dye. *Materials Today Communications* **2023**, *35*, No. 105883.
(8) Pathania, D.; Dhar, S.; Sharma, A.; Srivastava, A. K. Decolourization of Noxious Safranin-T from Waste Water Using Mangifera Indica as Precursor. *Environmental Sustainability* **2021**, *4* (2), 355−364.
(9) Abukhadra, M. R.; Mostafa, M.; El-Sherbeeny, A. M.; El-Meligy, M. A.; Nadeem, A. Instantaneous Adsorption of Synthetic Dyes from an Aqueous Environment Using Kaolinite Nanotubes: Equilibrium and Thermodynamic Studies. *ACS Omega* **2021**, *6* (1), 845−856.
(10) Mohamed, F.; Abukhadra, M. R.; Shaban, M. Removal of Safranin Dye from Water Using Polypyrrole Nanofiber/Zn-Fe Layered Double Hydroxide Nanocomposite (Ppy NF/Zn-Fe LDH) of Enhanced Adsorption and Photocatalytic Properties. *Science of The Total Environment* **2018**, *640−641*, 352−363.
(11) Eltaweil, A. S.; Ali Mohamed, H.; Abd El-Monaem, E. M.; El-Subruiti, G. M. Mesoporous Magnetic Biochar Composite for Enhanced Adsorption of Malachite Green Dye: Characterization, Adsorption Kinetics. *Thermodynamics and Isotherms. Advanced Powder Technology* **2020**, *31* (3), 1253−1263.
(12) Rabie, A. M.; Abukhadra, M. R.; Rady, A. M.; Ahmed, S. A.; Labena, A.; Mohamed, H. S. H.; Betiha, M. A.; Shim, J.-J. Instantaneous Photocatalytic Degradation of Malachite Green Dye under Visible Light Using Novel Green Co−ZnO/Algae Composites. *Res. Chem. Intermed.* **2020**, *46* (3), 1955−1973.
(13) Saad, A. M.; Abukhadra, M. R.; Abdel-Kader Ahmed, S.; Elzanaty, A. M.; Mady, A. H.; Betiha, M. A.; Shim, J.-J.; Rabie, A. M. Photocatalytic Degradation of Malachite Green Dye Using Chitosan Supported ZnO and Ce−ZnO Nano-Flowers under Visible Light. *Journal of Environmental Management* **2020**, *258*, No. 110043.
(14) Ofudje, E. A.; Adedapo, A. E.; Oladeji, O. B.; Sodiya, E. F.; Ibadin, F. H.; Zhang, D. Nano-Rod Hydroxyapatite for the Uptake of Nickel Ions: Effect of Sintering Behaviour on Adsorption Parameters. *Journal of Environmental Chemical Engineering* **2021**, *9* (5), No. 105931.
(15) Shahid, M.; Farooqi, Z. H.; Begum, R.; Arif, M.; Irfan, A.; Azam, M. Extraction of Cobalt Ions from Aqueous Solution by Microgels for In-Situ Fabrication of Cobalt Nanoparticles to Degrade Toxic Dyes: A Two Fold-Environmental Application. *Chem. Phys. Lett.* **2020**, *754*, No. 137645.
(16) Sayed, I. R.; Farhan, A. M.; AlHammadi, A. A.; El-Sayed, M. I.; Abd El-Gaied, I. M.; El-Sherbeeny, A. M.; Al Zoubi, W.; Ko, Y. G.; Abukhadra, M. R. Synthesis of Novel Nanoporous Zinc Phosphate/Hydroxyapatite Nano-Rods (ZPh/HPANRs) Core/Shell for Enhanced Adsorption of Ni2+ and Co2+ Ions: Characterization and Application. *J. Mol. Liq.* **2022**, *360*, No. 119527.
(17) Albukhari, S. M.; Salam, M. A.; Abukhadra, M. R. Effective Retention of Inorganic Selenium Ions (Se (VI) and Se (IV)) Using Novel Sodalite Structures from Muscovite; Characterization and Mechanism. *Journal of the Taiwan Institute of Chemical Engineers* **2021**, *120*, 116−126.
(18) Raju, CH. A. I.; Anitha, J.; Mahalakshmi Kalyani, R.; Satyanandam, K.; Jagadeesh, P. Sorption of Cobalt Using Marine Macro Seaweed Graciliariacorticatared Algae Powder. *Materials Today: Proceedings* **2021**, *44*, 1816−1827.
(19) Zhang, Y.; Hui, C.; Wei, R.; Jiang, Y.; Xu, L.; Zhao, Y.; Du, L.; Jiang, H. Study on Anionic and Cationic Dye Adsorption Behavior and Mechanism of Biofilm Produced by Bacillus Amyloliquefaciens DT. *Appl. Surf. Sci.* **2022**, *573*, No. 151627.
(20) Çiftçi, H. Removal of Methylene Blue from Water by Ultrasound-Assisted Adsorption Using Low-Cost Bentonites. *Chem. Phys. Lett.* **2022**, *802*, No. 139758.
(21) Alqahtani, M. D.; Nasser, N.; AlZahrani, S. A.; Allam, A. A.; Abukhadra, M. R. Characterization of Kaolinite Single Methoxy Nano-Sheets as Potential Carriers of Oxaliplatin Drug of Enhanced Loading, Release, and Cytotoxicity Properties During the Treatment of Colorectal Cancer. *Journal of Inorganic and Organometallic Polymers and Materials* **2023**, *33* (7), 2111−2126.
(22) Almahri, A. The Solid-State Synthetic Performance of Bentonite Stacked Manganese Ferrite Nanoparticles: Adsorption and Photo-Fenton Degradation of MB Dye and Antibacterial Applications. *Journal of Materials Research and Technology* **2022**, *17*, 2935−2949.
(23) Dardir, F. M.; Mohamed, A. S.; Abukhadra, M. R.; Ahmed, E. A.; Soliman, M. F. Cosmetic and Pharmaceutical Qualifications of Egyptian Bentonite and Its Suitability as Drug Carrier for Praziquantel Drug. *European Journal of Pharmaceutical Sciences* **2018**, *115*, 320−329.
(24) Alqahtani, M. D.; Nasser, N.; Bin Jumah, M. N.; AlZahrani, S. A.; Allam, A. A.; Abukhadra, M. R.; Bellucci, S. Insight into the Morphological Properties of Nano-Kaolinite (Nanoscrolls and Nanosheets) on Its Qualification as Delivery Structure of Oxaliplatin: Loading, Release, and Kinetic Studies. *Molecules* **2023**, *28* (13), 5158.
(25) Singh, R.; Dutta, S. The Role of pH and Nitrate Concentration in the Wet Chemical Growth of Nano-Rods Shaped ZnO Photocatalyst. *Nano-Structures & Nano-Objects* **2019**, *18*, 100250.
(26) Tan, D.; Yuan, P.; Dong, F.; He, H.; Sun, S.; Liu, Z. Selective Loading of 5-Fluorouracil in the Interlayer Space of Methoxy-Modified Kaolinite for Controlled Release. *Appl. Clay Sci.* **2018**, *159*, 102−106.
(27) Abukhadra, M. R.; Mohamed, A. S.; El-Sherbeeny, A. M.; Soliman, A. T. A. Enhanced Adsorption of Toxic and Biologically Active Levofloxacin Residuals from Wastewater Using Clay Nanotubes as a Novel Fixed Bed: Column Performance and Optimization. *ACS Omega* **2020**, *5* (40), 26195−26205.
(28) Guha, A.; Chattoraj, S. L.; Chatterjee, S.; Kumar, K. V.; Rao, P. V. N.; Bhaumik, A. K. Reflectance Spectroscopy-Guided Broadband Spectral Derivative Approach to Detect Glauconite-Rich Zones in Fossiliferous Limestone, Kachchh Region, Gujarat, India. *Ore Geol. Rev.* **2020**, *127*, No. 103825.
(29) Bruneel, Y.; Van Laer, L.; Brassinnes, S.; Smolders, E. Characterisation of the Highly Selective Caesium Sorption on Glauconite Rich Sands of Contrasting Geological Formations. *Appl. Geochem.* **2021**, *128*, No. 104926.
(30) Singla, R.; Alex, T. C.; Kumar, R. On Mechanical Activation of Glauconite: Physicochemical Changes, Alterations in Cation Exchange Capacity and Mechanisms. *Powder Technol.* **2020**, *360*, 337−351.
(31) Shmandiy, V.; Rigas, T.; Kharlamova, O.; Bezdeneznych, L. Research of Adsorption Properties of Glauconite-Based Composite Adsorbents. *Journal of Ecological Engineering* **2020**, *21* (6), 147−154.
(32) Abukhadra, M. R.; Bakry, B. M.; Adlii, A.; Yakout, S. M.; El-Zaidy, M. E. Facile Conversion of Kaolinite into Clay Nanotubes (KNTs) of Enhanced Adsorption Properties for Toxic Heavy Metals (Zn2+, Cd2+, Pb2+, and Cr6+) from Water. *Journal of Hazardous Materials* **2019**, *374*, 296−308.
(33) Franus; Bandura; Madej. Mono and Poly-Cationic Adsorption of Heavy Metals Using Natural Glauconite. *Minerals* **2019**, *9* (8), 470.
(34) Baldermann, A.; Banerjee, S.; Czuppon, G.; Dietzel, M.; Farkaš, J.; Löhr, S.; Moser, U.; Scheiblhofer, E.; Wright, N. M.; Zack, T. Impact of Green Clay Authigenesis on Element Sequestration in

https://doi.org/10.1021/acsomega.3c07870
ACS Omega 2023, 8, 49347−49361

Marine Settings. *Nat. Commun.* **2022**, *13* (1), 1527 DOI: 10.1038/s41467-022-29223-6.
(35) Pietsch, C.; Harrison, H. C.; Allmon, W. D. Whence the Gosport Sand (Upper Middle Eocene, Alabama)? The Origin of Glauconitic Shell Beds In the Paleogene of the U.S. Gulf Coastal Plain. *Journal of Sedimentary Research* **2016**, *86* (11), 1249−1268.
(36) El-Habaak, G.; Askalany, M.; Faraghaly, M.; Abdel-Hakeem, M. The Economic Potential of El-Gedida Glauconite Deposits, El-Bahariya Oasis, Western Desert. *Egypt. Journal of African Earth Sciences* **2016**, *120*, 186−197.
(37) Sobeih, M. M.; El-Shahat, M. F.; Osman, A.; Zaid, M. A.; Nassar, M. Y. Glauconite Clay-Functionalized Chitosan Nanocomposites for Efficient Adsorptive Removal of Fluoride Ions from Polluted Aqueous Solutions. *RSC Adv.* **2020**, *10* (43), 25567−25585.
(38) Moretto, L. M.; Orsega, E. F.; Mazzocchin, G. A. Spectroscopic Methods for the Analysis of Celadonite and Glauconite in Roman Green Wall Paintings. *Journal of Cultural Heritage* **2011**, *12* (4), 384−391.
(39) Shawky, A.; El-Sheikh, S. M.; Rashed, M. N.; Abdo, S. M.; El-Dosoqy, T. I. Exfoliated Kaolinite Nanolayers as an Alternative Photocatalyst with Superb Activity. *Journal of Environmental Chemical Engineering* **2019**, *7* (3), No. 103174.
(40) Younes, H.; El-Etriby, H. Kh.; Mahanna, H. High Removal Efficiency of Reactive Yellow 160 Dye from Textile Wastewater Using Natural and Modified Glauconite. *International Journal of Environmental Science and Technology* **2022**, *19* (6), 5659−5674.
(41) Salam, M. A.; Abukhadra, M. R.; Mostafa, M. Effective Decontamination of As(V), Hg(II), and U(VI) Toxic Ions from Water Using Novel Muscovite/Zeolite Aluminosilicate Composite: Adsorption Behavior and Mechanism. *Environmental Science and Pollution Research* **2020**, *27* (12), 13247−13260.
(42) Kumar, U.; Bandayopadhyay, M. Sorption of Cadmium from Aqueous Solution Using Pretreated Rice Husk. *Bioresour. Technol.* **2006**, *97* (1), 104−109.
(43) Yuan, P.; Tan, D.; Annabi-Bergaya, F.; Yan, W.; Liu, D.; Liu, Z. From Platy Kaolinite to Aluminosilicate Nanoroll via One-Step Delamination of Kaolinite: Effect of the Temperature of Intercalation. *Appl. Clay Sci.* **2013**, *83*−*84*, 68−76.
(44) Vivas, E. L.; Cho, K. Efficient Adsorptive Removal of Cobalt(II) Ions from Water by Dicalcium Phosphate Dihydrate. *Journal of Environmental Management* **2021**, *283*, No. 111990.
(45) El-Zahhar, A. A.; Awwad, N. S. Removal of Malachite Green Dye from Aqueous Solutions Using Organically Modified Hydroxyapatite. *Journal of Environmental Chemical Engineering* **2016**, *4* (1), 633−638.
(46) Zhang, F.; Ma, B.; Jiang, X.; Ji, Y. Dual Function Magnetic Hydroxyapatite Nanopowder for Removal of Malachite Green and Congo Red from Aqueous Solution. *Powder Technol.* **2016**, *302*, 207−214.
(47) Lee, Y.-C.; Kim, J.-Y.; Shin, H.-J. Removal of Malachite Green (MG) From Aqueous Solutions by Adsorption, Precipitation, and Alkaline Fading Using Talc. *Sep. Sci. Technol.* **2013**, *48* (7), 1093−1101.
(48) Chen, Y.; Nie, Z.; Gao, J.; Wang, J.; Cai, M. A Novel Adsorbent of Bentonite Modified Chitosan-Microcrystalline Cellulose Aerogel Prepared by Bidirectional Regeneration Strategy for Pb(II) Removal. *Journal of Environmental Chemical Engineering* **2021**, *9* (4), No. 105755.
(49) Tran, T. N.; Do, Q. C.; Kim, D.; Kim, J.; Kang, S. Urchin-like Structured Magnetic Hydroxyapatite for the Selective Separation of Cerium Ions from Aqueous Solutions. *Journal of Hazardous Materials* **2022**, *430*, No. 128488.
(50) El Qada, E. Kinetic Behavior of the Adsorption of Malachite Green UsingJordanian Diatomite as Adsorbent. *JORDANIAN JOURNAL OF ENGINEERING AND CHEMICAL INDUSTRIES (JJECI)* **2020**, *3* (1), 1−10.
(51) Lin, X.; Xie, Y.; Lu, H.; Xin, Y.; Altaf, R.; Zhu, S.; Liu, D. Facile Preparation of Dual La-Zr Modified Magnetite Adsorbents for Efficient and Selective Phosphorus Recovery. *Chemical Engineering Journal* **2021**, *413*, No. 127530.
(52) Jiang, Y.; Abukhadra, M. R.; Refay, N. M.; Sharaf, M. F.; El-Meligy, M. A.; Awwad, E. M. Synthesis of Chitosan/MCM-48 and β-Cyclodextrin/MCM-48 Composites as Bio-Adsorbents for Environmental Removal of Cd2+ Ions; Kinetic and Equilibrium Studies. *React. Funct. Polym.* **2020**, *154*, No. 104675.
(53) Sherlala, A. I. A.; Raman, A. A. A.; Bello, M. M.; Buthiyappan, A. Adsorption of Arsenic Using Chitosan Magnetic Graphene Oxide Nanocomposite. *Journal of Environmental Management* **2019**, *246*, 547−556.
(54) Huang, Y.; Zeng, X.; Guo, L.; Lan, J.; Zhang, L.; Cao, D. Heavy Metal Ion Removal of Wastewater by Zeolite-Imidazolate Frameworks. *Sep. Purif. Technol.* **2018**, *194*, 462−469.
(55) Jasper, E. E.; Ajibola, V. O.; Onwuka, J. C. Nonlinear Regression Analysis of the Sorption of Crystal Violet and Methylene Blue from Aqueous Solutions onto an Agro-Waste Derived Activated Carbon. *Appl. Water Sci.* **2020**, *10* (6), 132 DOI: 10.1007/s13201-020-01218-y.
(56) Giles, C. H.; MacEwan, T. H.; Nakhwa, S. N.; Smith, D. 786. Studies in Adsorption. Part XI. A System of Classification of Solution Adsorption Isotherms, and Its Use in Diagnosis of Adsorption Mechanisms and in Measurement of Specific Surface Areas of Solids. *Journal of the Chemical Society (Resumed)* **1960**, 3973.
(57) Abukhadra, M. R.; Dardir, F. M.; Shaban, M.; Ahmed, E. A.; Soliman, M. F. Superior Removal of Co2+, Cu2+ and Zn2+ Contaminants from Water Utilizing Spongy Ni/Fe Carbonate−Fluorapatite; Preparation, Application and Mechanism. *Ecotoxicology and Environmental Safety* **2018**, *157*, 358−368.
(58) Shaban, M.; Abukhadra, M. R.; Shahien, M. G.; Khan, A. A. P. Upgraded Modified Forms of Bituminous Coal for the Removal of Safranin-T Dye from Aqueous Solution. *Environmental Science and Pollution Research* **2017**, *24* (22), 18135−18151.
(59) Faisal, M. L. F. M. Batch Sorption of Copper (II) Ions from Simulated Aqueous Solution by Banana Peel. *Al-Khwarizmi Eng. J.* **2017**, *12* (4), 117−125.
(60) Mobarak, M.; Ali, R. A. M.; Seliem, M. K. Chitosan/Activated Coal Composite as an Effective Adsorbent for Mn(VII): Modeling and Interpretation of Physicochemical Parameters. *Int. J. Biol. Macromol.* **2021**, *186*, 750−758.
(61) Ashraf, M.-T.; AlHammadi, A. A.; El-Sherbeeny, A. M.; Alhammadi, S.; Al Zoubi, W.; Ko, Y. G.; Abukhadra, M. R. Synthesis of Cellulose Fibers/Zeolite-A Nanocomposite as an Environmental Adsorbent for Organic and Inorganic Selenium Ions; Characterization and Advanced Equilibrium Studies. *J. Mol. Liq.* **2022**, *360*, No. 119573.
(62) Dhaouadi, F.; Sellaoui, L.; Reynel-Ávila, H. E.; Landín-Sandoval, V.; Mendoza-Castillo, D. I.; Jaime-Leal, J. E.; Lima, E. C.; Bonilla-Petriciolet, A.; Lamine, A. B. Adsorption Mechanism of Zn2+, Ni2+, Cd2+, and Cu2+ Ions by Carbon-Based Adsorbents: Interpretation of the Adsorption Isotherms via Physical Modelling. *Environmental Science and Pollution Research* **2021**, *28* (24), 30943−30954.
(63) Sellaoui, L.; Ali, J.; Badawi, M.; Bonilla-Petriciolet, A.; Chen, Z. Understanding the Adsorption Mechanism of Ag+ and Hg2+ on Functionalized Layered Double Hydroxide via Statistical Physics Modeling. *Appl. Clay Sci.* **2020**, *198*, No. 105828.
(64) Ali, R. A. M.; Mobarak, M.; Badawy, A. M.; Lima, E. C.; Seliem, M. K.; Ramadan, H. S. New Insights into the Surface Oxidation Role in Enhancing Congo Red Dye Uptake by Egyptian Ilmenite Ore: Experiments and Physicochemical Interpretations. *Surfaces and Interfaces* **2021**, *26*, No. 101316.
(65) Dhaouadi, F.; Sellaoui, L.; Badawi, M.; Reynel-Ávila, H. E.; Mendoza-Castillo, D. I.; Jaime-Leal, J. E.; Bonilla-Petriciolet, A.; Lamine, A. B. Statistical Physics Interpretation of the Adsorption Mechanism of Pb2+, Cd2+ and Ni2+ on Chicken Feathers. *J. Mol. Liq.* **2020**, *319*, No. 114168.
(66) Shemy, M. H.; Othman, S. I.; Alfassam, H. E.; Al-Waili, M. A.; Alqhtani, H. A.; Allam, A. A.; Abukhadra, M. R. Synthesis of Green

https://doi.org/10.1021/acsomega.3c07870
ACS Omega 2023, 8, 49347−49361

Magnetite/Carbonized Coffee Composite from Natural Pyrite for Effective Decontamination of Congo Red Dye: Steric, Synergetic, Oxidation, and Ecotoxicity Studies. *Catalysts* **2023**, *13* (2), 264.
(67) Sellaoui, L.; Guedidi, H.; SarraWjihi, S.; Reinert, L.; Knani, S.; Duclaux, L.; Ben Lamine, A. Experimental and Theoretical Studies of Adsorption of Ibuprofen on Raw and Two Chemically Modified Activated Carbons: New Physicochemical Interpretations. *RSC Adv.* **2016**, *6* (15), 12363−12373.
(68) Zafar, M. N.; Amjad, M.; Tabassum, M.; Ahmad, I.; Zubair, M. SrFe2O4 Nanoferrites and SrFe2O4/Ground Eggshell Nanocomposites: Fast and Efficient Adsorbents for Dyes Removal. *Journal of Cleaner Production* **2018**, *199*, 983−994.
(69) Yildirim, A.; Bulut, Y. Adsorption Behaviors of Malachite Green by Using Crosslinked Chitosan/Polyacrylic Acid/Bentonite Composites with Different Ratios. *Environmental Technology & Innovation* **2020**, *17*, No. 100560.
(70) Jiang, M.; Chen, L.; Niu, N. Enhanced Adsorption for Malachite Green by Functionalized Lignin Magnetic Composites: Optimization, Performance and Adsorption Mechanism. *J. Mol. Struct.* **2022**, *1260*, No. 132842.
(71) Gupta, K.; Khatri, O. P. Reduced Graphene Oxide as an Effective Adsorbent for Removal of Malachite Green Dye: Plausible Adsorption Pathways. *J. Colloid Interface Sci.* **2017**, *501*, 11−21.
(72) Sricharoen, P.; Kongsri, S.; Kukusamude, C.; Areerob, Y.; Nuengmatcha, P.; Chanthai, S.; Limchoowong, N. Ultrasound-Irradiated Synthesis of 3-Mercaptopropyl Trimethoxysilane-Modified Hydroxyapatite Derived from Fish-Scale Residues Followed by Ultrasound-Assisted Organic Dyes Removal. *Sci. Rep.* **2021**, *11* (1), 5560 DOI: 10.1038/s41598-021-85206-5.
(73) Zaidi, N. A. H. M.; Lim, L. B. L.; Usman, A. Enhancing Adsorption of Malachite Green Dye Using Base-Modified Artocarpus Odoratissimus Leaves as Adsorbents. *Environmental Technology & Innovation* **2019**, *13*, 211−223.
(74) Gao, M.; Wang, Z.; Yang, C.; Ning, J.; Zhou, Z.; Li, G. Novel Magnetic Graphene Oxide Decorated with Persimmon Tannins for Efficient Adsorption of Malachite Green from Aqueous Solutions. *Colloids Surf., A* **2019**, *566*, 48−57.
(75) Raval, N. P.; Shah, P. U.; Shah, N. K. Malachite Green "a Cationic Dye" and Its Removal from Aqueous Solution by Adsorption. *Applied Water Science* **2017**, *7* (7), 3407−3445.

https://doi.org/10.1021/acsomega.3c07870
ACS Omega 2023, 8, 49347−49361